

## Elves and associated electron density changes due to cloud-to-ground and in-cloud lightning discharges

R. A. Marshall,<sup>1</sup> U. S. Inan,<sup>1</sup> and V. S. Glukhov<sup>1,2</sup>

Received 18 May 2009; revised 23 October 2009; accepted 30 October 2009; published 3 April 2010.

[1] A 3-D finite difference time domain model is used to simulate the lightning electromagnetic pulse (EMP) and its interaction with the lower ionosphere. Results agree with the frequently observed, doughnut-shaped optical signature of elves but show that the structure exhibits asymmetry due to the presence of Earth's ambient magnetic field. Furthermore, in-cloud (horizontal) lightning channels produce observable optical emissions without the doughnut shape and, in fact, produce a much stronger optical output for the same channel current. Electron density perturbations associated with elves are also calculated, with contributions from attachment and ionization. Results presented as a function of parameters such as magnetic field direction, dipole current orientation, altitude and amplitude, and ambient ionospheric density profile demonstrate the highly nonlinear nature of the EMP-ionosphere interaction. Ionospheric effects of a sequence of in-cloud discharges are calculated, simulating a burst of in-cloud lightning activity and resulting in large density changes in the overlying ionosphere.

**Citation:** Marshall, R. A., U. S. Inan, and V. S. Glukhov (2010), Elves and associated electron density changes due to cloud-to-ground and in-cloud lightning discharges, *J. Geophys. Res.*, *115*, A00E17, doi:10.1029/2009JA014469.

### 1. Introduction

[2] First observed from the Space Shuttle in 1991 [Boeck *et al.*, 1992], elves are the optical signature of the lightning electromagnetic pulse (EMP) interaction with the lower ionosphere. These bright ( $>1$  MR), short-duration ( $<1$  ms) optical flashes have since been frequently observed from the ground and from satellites [Fukunishi *et al.*, 1996; Barrington-Leigh *et al.*, 1999; Mende *et al.*, 2005a]. Most observed elves have a “doughnut” shape with a null at the center, which is a result of the radiation pattern of cloud-to-ground lightning, that of a vertical monopole antenna over a conducting ground plane.

[3] Inan *et al.* [1991] was the first to calculate ionospheric density changes due to lightning EMP, through secondary ionization by heated electrons. Taranenko *et al.* [1993a, 1993b] used a 1-D time domain model to calculate direct ionization due to the EMP fields, as well as optical emissions, using empirical and kinetic models of the interactions, respectively. However, this 1-D model did not take into account the radiation pattern from horizontal versus vertical lightning discharges. Rowland *et al.* [1996] used a so-called “2 1/2 D” model of the EMP-ionosphere interaction and were the first to separately simulate vertical and horizontal discharges. Inan *et al.* [1996] used a 2-D cylindrically

symmetric model to simulate the radiation fields and resulting ionospheric effects of a vertical discharge. Veronis *et al.* [1999] and Barrington-Leigh *et al.* [2001] extended this 2-D model to include effects of the quasi-electrostatic field (i.e., induction field) resulting from slow ( $\sim 500$   $\mu$ s) currents. The first 3-D model was presented by Cho and Rycroft [2001] in an attempt to simulate in-cloud lightning and its effect on the ionosphere. However, that model was only able to simulate sinusoidally varying in-cloud currents, and did not include the effects of the Earth's magnetic field.

[4] Results of these models of the lightning EMP-ionosphere interaction have been consistent with observations. However, these models have all been either 1-D or 2-D with cylindrical symmetry, and have not included the effects of the Earth's ambient magnetic field  $B_0$ , nor have they been able to simulate horizontal lightning channels. In this paper we present results of the first fully 3-D time domain model of the EMP interaction with the ionosphere. The use of this model was prompted by possible observations of elves exhibiting an asymmetry in the azimuthal intensity. Furthermore, with this 3-D model we simulate horizontal lightning channels and calculate their possible effects in the ionosphere.

[5] Note that Krider [1992, 1994], using a transmission line (TL) model, predicted an enhancement of the radiation field at high elevation angles (i.e., near vertical) for very high return stroke speeds (near the speed of light), meaning the dipole radiation pattern is no longer accurate. Rakov and Tuni [2003] and Lu [2006] used a similar TL model, as well as a modified TL model with exponential current decay with height (an MTLE model), to predict electric field amplitudes at 90 km altitude from cloud-to-ground lightning dis-

<sup>1</sup>Space, Telecommunications and Radioscience Laboratory, Stanford University, Stanford, California, USA.

<sup>2</sup>Permanently at Liquidnet Holdings, Inc., New York, New York, USA.

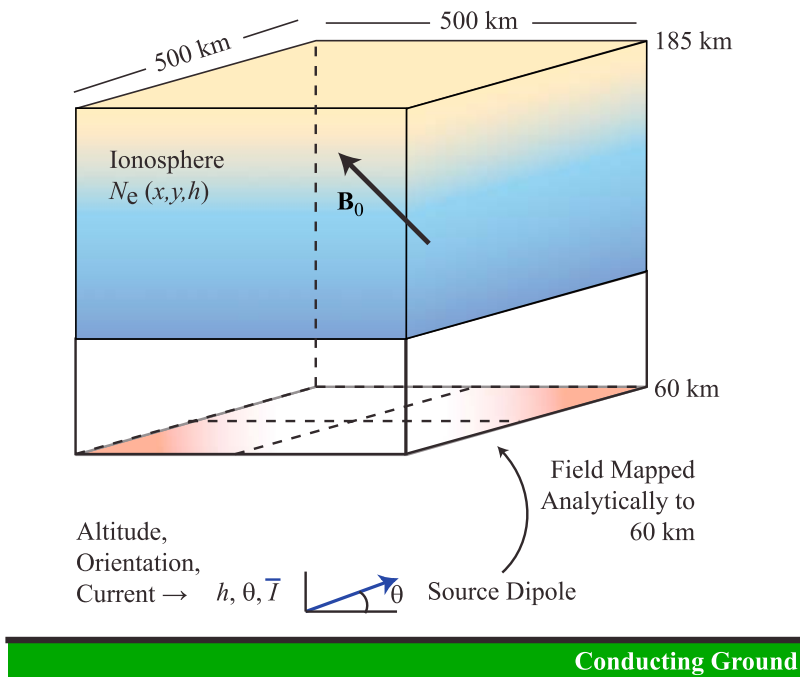


**Figure 1.** Simulation space used in the EMP model. Fields are calculated analytically at the lower boundary for an arbitrarily oriented dipole and then propagated into the simulation space using equations (4)–(6).

charges, with fields up to 10–15 V/m from a 72 kA discharge, consistent with observations of elves.

## 2. The 3-D EMP Model

[6] The present 3-D model is designed to simulate two effects that cannot be observed in 1-D or 2-D models. Namely, we aim to account for the Earth’s magnetic field, and to quantify the effects of in-cloud lightning on the lower ionosphere; both of these effects require a 3-D model. In a Cartesian 2-D model, any source currents would be infinite in the third dimension, thus representing an unrealistic “infinitely long wire” source current. In a cylindrical 2-D model, a finite-length vertical current can be simulated, but horizontal currents require a drain to the ground [e.g., *Hu et al., 2007*].

[7] The finite difference time domain (FDTD) method is used to simulate the propagation of EMP pulses and their interaction with the lower ionosphere. The simulation space is shown in Figure 1. The space is Cartesian and extends 500 km in the  $x$  and  $y$  directions, and from as low as 50 km to as high as 195 km in altitude; these altitudes are easily adjustable. For the simulation results shown in this work, the altitude range of 60–185 km is used, with the grid having unit cells of  $(\Delta x, \Delta y, \Delta z) = (2, 2, 0.8)$  km, and  $\Delta t = 0.025 \Delta z/c$ . This choice of  $\Delta t$  ensures stability for phase velocities  $v_p$  as low as  $c/40$ ; these simulations involve waves with  $0.1 c \leq v_p \leq c$ .

[8] The model uses a simple second-order Mur absorbing boundary condition (ABC) [*Mur, 1981*] on the lower boundary at 60 km to absorb waves reflected from the lower ionosphere back toward to lower boundary. The sides and top of the simulation space do not have ABCs, and are

instead placed far enough away that reflections do not affect the results during the time of observations. In an anisotropic medium such as a magnetized plasma, phase and group velocity vectors can have antiparallel components into and out of the boundary, which causes most forms of ABCs to amplify, rather than absorb, incident waves; this phenomenon is described in full by *Chevalier et al. [2008]*. We place the boundaries far enough from the source to avoid such problems, at the expense of computational time and memory.

[9] The source fields at the 60 km lower boundary are calculated analytically at each time step and are used as an “input” to the model. This procedure eliminates the quasi-electrostatic (QE) field component due to charge transfer, isolating the effect of EMP. It furthermore reduces the size of the computation space, and circumvents a problem in

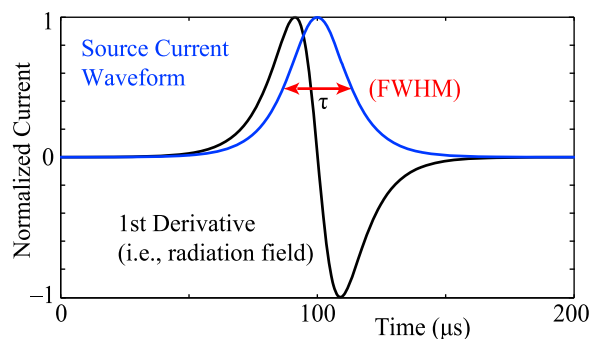


**Figure 2.** Source current waveform used in all simulations. For a pulse with  $1/\tau = 10^5$ , the FWHM is  $\sim 26 \mu\text{s}$ , which we refer to for simplicity as a “20  $\mu\text{s}$  pulse.”

some FDTD models where the finite current channel size can only be as small as the grid cell (i.e., 2 km wide, an unrealistic current channel). The equations to solve at the boundary are radiation equations for a small dipole, found in many textbooks, typically written in the frequency domain for a  $z$ -directed current. In the formulation herein, the time domain versions of these equations are used, which are derived from the Hertz dipole vectors of *Budden* [1961, p. 43]:

$$E_r = \frac{1}{2\pi\epsilon_0} \sin\theta \left( \frac{[M]}{r^3} + \frac{1}{cr^2} \frac{\partial[M]}{\partial t} \right) \quad (1)$$

$$E_\theta = \frac{1}{4\pi\epsilon_0} \cos\theta \left( \frac{[M]}{r^3} + \frac{1}{cr^2} \frac{\partial[M]}{\partial t} + \frac{1}{c^2 r} \frac{\partial^2[M]}{\partial t^2} \right) \quad (2)$$

$$H_\phi = \frac{1}{4\pi\epsilon_0} \cos\theta \left( \frac{1}{cr^2} \frac{\partial[M]}{\partial t} + \frac{1}{c^2 r} \frac{\partial^2[M]}{\partial t^2} \right) \quad (3)$$

$$E_\phi = H_r = H_\theta = 0$$

where  $[M]$  denotes the “retarded” value of the dipole moment  $M$ ,  $d\mathbf{M}/dt = i\mathbf{l}$ , and  $i$  and  $\mathbf{l}$  are the current magnitude and current channel vector, respectively; thus for a given  $M(t)$ ,  $[M] = M(t - r/c)$ .

[10] To solve for a dipole of arbitrary orientation ( $x$ ,  $y$  and  $z$  components), these equations are simply solved for each component, and for the  $x$  and  $y$  components a rotation is applied to the results. For the simulations presented here, the current is modeled by  $I(t) = I_0 \cosh^{-1}(t/\tau)$ , shown in Figure 2, where  $I_0$  is the amplitude in kA and where the parameter  $\tau$  controls the temporal width of the current pulse. This analytical form is not strictly accurate as a lightning return stroke, but is chosen for its simple analytical forms to use in equations (1)–(3). Furthermore, by converting the input amplitude to units of  $E_{100}$  (see equation (15)), we force the fields to have realistic amplitudes in the ionosphere regardless of the current waveform.

## 2.1. Update Equations

[11] The EMP model self-consistently solves Maxwell’s equations and the Langevin equation:

$$\nabla \times \bar{\mathbf{E}}_w = -\mu_0 \frac{\partial \bar{\mathbf{H}}_w}{\partial t} \quad (4)$$

$$\frac{\partial \bar{\mathbf{J}}}{\partial t} + \nu \bar{\mathbf{J}} = \epsilon_0 \omega_p^2 \bar{\mathbf{E}}_w + \bar{\omega}_b \times \bar{\mathbf{J}} \quad (5)$$

$$\nabla \times \bar{\mathbf{H}}_w = \epsilon_0 \frac{\partial \bar{\mathbf{E}}_w}{\partial t} + \bar{\mathbf{J}} \quad (6)$$

where the subscript  $w$  is used to denote the wave electric and magnetic fields (in contrast to the Earth’s static magnetic field  $\mathbf{B}_0$ );  $\omega_p = \sqrt{N_e q^2 / m_e \epsilon_0}$  is the electron plasma frequency for an electron density  $N_e$ ,  $\bar{\omega}_b = q_e \mathbf{B}_0 / m_e$  is the electron gyrofrequency, and  $\nu$  is the effective electron collision frequency. Equations (4) and (6) are discretized with

second-order centered differences in time and space. Equation (5) is discretized using a modified version of the “TRISTAN” algorithm presented by *Buneman* [1993]. In this algorithm, the solution of (5) is separated into the “natural” and “forced” components, and the forces on the right are labeled “acceleration” (the  $\epsilon_0 \omega_p^2 \bar{\mathbf{E}}$  term) and “rotation” (the  $\omega_b \times \bar{\mathbf{J}}$  term).

## 2.2. Collision Frequency

[12] The nighttime ionosphere has an electron density that increases exponentially with altitude beginning around 65 km. At this altitude and above, the electron mobility  $\mu_e$  dominantly determines the overall conductivity of the ionosphere, which is given by  $\sigma = q_e N_e \mu_e + \sum_{\text{ions}} q_i N_i \mu_i$ . Typical electron densities as a function of altitude are shown in Figure 3, along with atmospheric density versus altitude. In most of the simulations in this work Profile #2 is used, but the effects of different electron density profiles are also investigated.

[13] The presence of collisions ( $\nu$ ) and the Earth’s magnetic field ( $\bar{\omega}_b = q_e \mathbf{B}_0 / m_e$ ) in equation (5) both modify the electron motion in the presence of the wave electric field  $\bar{\mathbf{E}}$ . Electrons and ions gyrate around Earth’s magnetic field lines with angular frequency  $\omega_c$ , except when the collision frequency  $\nu$  becomes comparable to or larger than  $\omega_c$ , in which case the gyromotion becomes regularly interrupted. The “effective electric field” of the incident wave that is applied to such electrons is given, in phasor form, by [*Gurevich*, 1978, p. 75, equation (2.169)]

$$\mathbf{E}_{\text{eff}}^2 = \mathbf{E}_{\parallel}^2 + (\omega^2 + \nu^2) \left[ \frac{\mathbf{E}_{\perp-}^2}{(\omega - \omega_c)^2 + \nu^2} + \frac{\mathbf{E}_{\perp+}^2}{(\omega + \omega_c)^2 + \nu^2} \right] \quad (7)$$

where  $\mathbf{E}_{\parallel}$  is the component of the wave electric field parallel to  $B_0$ ,  $\mathbf{E}_{\perp-}$  and  $\mathbf{E}_{\perp+}$  are the perpendicular components of the electric field which rotate with and against the electron gyromotion, and  $\nu$  is a kinetically calculated effective collision frequency [*Glukhov and Inan*, 1996]. In the simulations described here, the frequency  $\omega$  ( $\leq 100$  kHz) is always much less than the gyrofrequency  $\omega_c$  ( $\sim 0.7$ – $1.8$  MHz at 100 km altitude, depending on latitude), so that equation (7) reduces to

$$\mathbf{E}_{\text{eff}}^2 = \mathbf{E}_{\parallel}^2 + \mathbf{E}_{\perp}^2 \frac{\nu^2}{\nu^2 + \omega_c^2} \quad (8)$$

[14] Note that equation (8) is independent of wave frequency. Electron motion is also damped by collisions with neutrals, given by the second term in equation (5). The rate of collisions between electrons and neutrals is given by  $\nu = q_e / (\mu_e m_e)$ , where  $\mu_e$  is the electron mobility. Laboratory data on electron swarms from *Davies* [1983] demonstrate that the mobility is a nonlinear function of the so-called reduced electric field  $E_{\text{eff}}/N$ , where in this case  $E_{\text{eff}}$  is the magnitude of the “effective” electric field calculated above, and  $N$  is the neutral atmospheric density. The data from *Davies* [1983] and the analytical fit used herein are shown in Figure 3b. The mobility takes a maximum value of  $1.36 N_0 / N \text{ m}^2 \text{ V}^{-1} \text{ s}^{-1}$  in the thermal limit, i.e., for small applied fields. In our

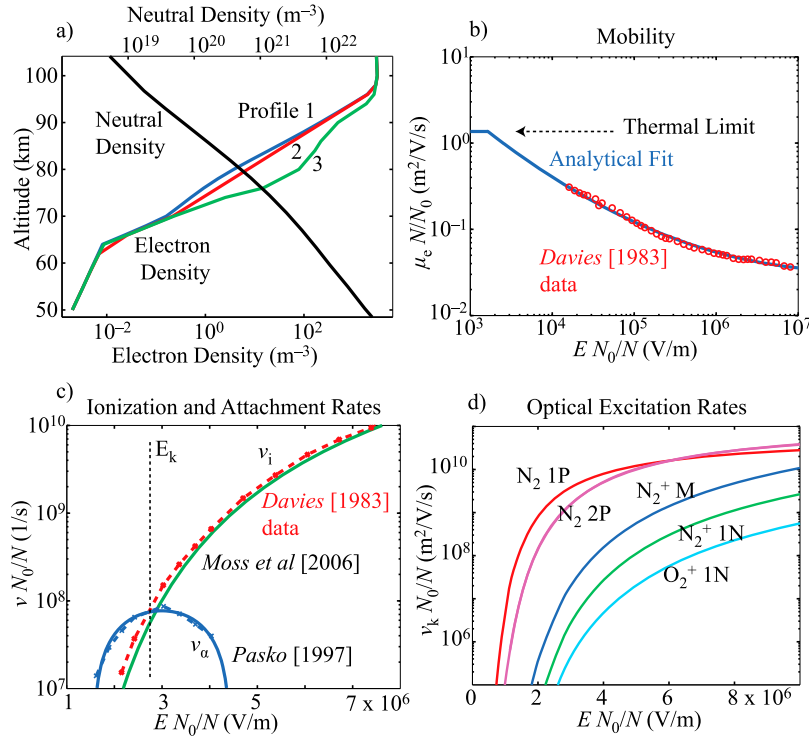


**Figure 3.** (a) Electron and neutral density profiles, (b) mobility as a function of reduced electric field, (c) ionization and attachment rates as a function of reduced electric field, and (d) optical excitation rates as a function of reduced electric field.

model, the mobility is updated self-consistently at each point in time and space as the fields propagate.

### 2.3. Ionization, Attachment, and Optical Emissions

[15] Ionization occurs when an electron with sufficient energy collides inelastically with a neutral molecule and creates an extra free electron. In the atmosphere dominated by nitrogen and oxygen, ionization can be characterized by the reaction  $M_2 + e^- + \text{energy} \rightarrow M_2^+ + 2e^-$ , where  $M_2$  represents either  $N_2$  or  $O_2$ , and the energy required for ionization is 12.06 eV for oxygen or 15.60 eV for nitrogen [Moss et al., 2006]. The number of ionization events that occur in a volume of air per unit time similarly depends on the reduced electric field  $E_{\text{eff}}/N$ .

[16] The results of laboratory experiments and numerical models, yielding the ionization rate  $\nu_i$  as a function of reduced electric field, are summarized in Figure 3. Davies [1983] presents results of laboratory swarm experiments for a range of electric fields, and recognizes that these rates scale with the air density  $N$ . Papadopoulos et al. [1993] gives an analytical fit to kinetic calculations. Moss et al. [2006] presented kinetic calculations using a numerical solution to the electron distribution function (using a code known as ELENDF [see Morgan and Penetrante, 1990]) and Monte Carlo simulations, and these are compared to empirical ionization rates given by Aleksandrov et al. [1995]. In this work we use the analytical expression given by Papadopoulos et al. [1993]:

$$\nu_i = 7.6 \times 10^{-13} N x^2 f(x) e^{-4.7(\frac{1}{x}-1)} \quad (9)$$

where

$$f(x) = \frac{2}{3} \left( 1 + 6.3 e^{-2.6/x} \right) \quad \text{and} \quad x = E_{\text{eff}}/E_k \quad (10)$$

[17] The breakdown field  $E_k$  in  $V\text{-m}^{-1}$  is given by Papadopoulos et al. [1993], which at low frequencies can be approximated by  $E_k = 3.2 \times 10^6 N/N_0$  with  $N_0 = 2.688 \times 10^{25} m^{-3}$ . Note that the breakdown field depends on frequency; for the results described here, the number density  $N \simeq 10^{19} m^{-3}$  at 100 km altitude (the highest altitude of interest; see Figure 3), and the term under the square root sign can be ignored for all frequencies even into the MHz range. Note that at 90 km altitude,  $N \simeq 7 \times 10^{19} m^{-3}$ , and the breakdown field is  $E_k \simeq 8.3 V\text{-m}^{-1}$ .

[18] Electrons are removed via dissociative attachment to molecular oxygen, given by the reaction  $O_2 + e^- + 3.7 \text{ eV} \rightarrow O + O^-$ . The attachment rate similarly depends on the reduced electric field  $E_{\text{eff}}/N$ . Figure 3c shows rates from a number of sources. Davies [1983] again provides rates determined from electron swarm experiments, while Pasko et al. [1997] provides empirical fits to this data.

[19] The low-energy approximation from Pasko et al. [1997] is used in this work. This model has been shown to underestimate the attachment rate at higher energies; however, at these high energies ionization overwhelms attachment, so that an accurate calculation of the attachment rate is not necessary. The breakdown field  $E_k$  is shown in Figure 3, as the field where the ionization and attachment rates are equal; above this field value, avalanche ionization

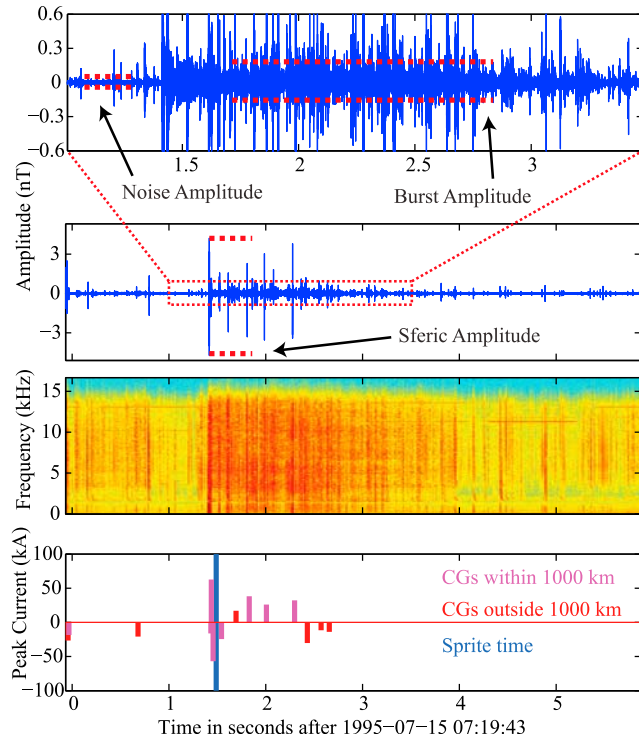


**Figure 4.** Measurement of relative spheric and burst amplitudes. The first and second panels show time series VLF data and the process of measuring the burst envelope amplitude. The third panel shows the spheric burst in spectrogram form, and the fourth panel shows the NLDN lightning data for CG strokes.

occurs, so that the electron density continues to grow as long the electric field is applied.

[20] After calculating the effective electric field at a given location in space at a particular time step, the electron density is updated via the simple differential equation:

$$\frac{dN_e}{dt} = \underbrace{(\nu_i - \nu_a)}_{\nu_{\text{tot}}} N_e - \alpha N_e^2 \quad (11)$$

where  $\nu_a$  is the attachment rate and  $\alpha$  is an effective three-body recombination coefficient, which is assumed to be zero in this model.

[21] Optical emissions are calculated for the  $N_2$  first positive ( $B^3\Pi_g \rightarrow A^3\Sigma_u$ ),  $N_2$  second positive ( $C^3\Pi_u \rightarrow B^3\Pi_g$ ),  $N_2^+$  first negative ( $B^2\Sigma_u^+ \rightarrow X^2\Sigma_g^+$ ),  $O_2^+$  first negative ( $b^4\Sigma_g^- \rightarrow a^4\Pi_u$ ), and  $N_2^+$  Meinel ( $A^2\Pi \rightarrow X^2\Sigma_g^+$ ) band systems. The optical excitation rates for these band systems are evaluated for a range of electric fields  $E_{\text{eff}}$  and neutral densities  $N$  using the rates calculated by *Moss et al.* [2006] using the ELENDF code. The excitation rates are shown in Figure 3 as a function of the reduced electric field.

[22] To determine the photon output, the number of molecules  $n_k$  in the excited state  $k$  corresponding to the band system of interest must be determined; for instance, for the  $N_2$  1P band system, the number of  $N_2$  molecules in the

$B^3\Pi_g$  state is calculated, which is governed by the relation [*Sipler and Biondi, 1972*]

$$\frac{\partial n_k}{\partial t} = \nu_k N_e - \frac{n_k}{\tau_k} + \sum_m n_m A_m \quad (12)$$

where  $\tau_k$  is the total lifetime of state  $k$  and is given by  $\tau_k^{-1} = A_k + \alpha_1 N_{N_2} + \alpha_2 N_{O_2}$ ;  $\alpha_1$  and  $\alpha_2$  are the quenching rates due to collisions with  $N_2$  and  $O_2$  molecules, and  $N_{N_2}$  and  $N_{O_2}$  are the densities of nitrogen and oxygen molecules. The term  $\sum_m n_m A_m$  represents an increase in  $n_k$  due to cascading from higher states; for example, cascading from  $C^3\Pi_u$  to  $B^3\Pi_g$  (through the  $N_2$  2P emission) leaves an extra molecule in the  $B^3\Pi_g$  state available for the  $N_2$  1P emission. The coefficients for the band systems under consideration are given by *Pasko et al.* [1997, Table 1].  $N_2$  1P is primarily quenched by collisions with nitrogen, while  $N_2$  2P is primarily quenched by collisions with oxygen.

[23] Since the lifetimes of these states are very fast ( $\sim$ ns to a few  $\mu$ s) compared to the rate of change of the electric field (tens to hundreds of  $\mu$ s), it is assumed that the instantaneous population  $n_k$  of excited state  $k$  is constant, so that  $dn_k/dt = 0$ , and the solution of (12) is

$$n_k = \frac{\nu_k N_e + \sum_m n_m A_m}{A_k + \alpha_1 N_{N_2} + \alpha_2 N_{O_2}} \quad (13)$$

[24] Finally, the intensity in Rayleighs measured by an observer is given by

$$I_k = 10^{-6} \int_L A_k n_k dl \quad (14)$$

where the integral is taken along  $L$ , the line of sight from the source to an observer.

## 2.4. Determining In-Cloud Pulse Amplitudes

[25] In this section, estimates are discussed for the amplitudes of the input source current. While currents for cloud-to-ground discharges can be directly measured, direct measurements for in-cloud lightning are far more difficult. An accurate estimate of realistic in-cloud discharge current amplitudes is critical for realistic simulations, since, as is evident from the ionization and attachment rates above, both effects are highly nonlinear. Measurements of in-cloud current pulse amplitudes are sparse in the lightning literature. *Smith et al.* [1999] reports an average  $E_{100}$  of  $9.5 \text{ V m}^{-1}$  for narrow bipolar pulses (NBPs), but similar measurements for ordinary intracloud discharges or spider lightning are not available.  $E_{100}$  is defined by *Uman and McLain* [1970] and *Orville* [1991] as the electric field measured at 100 km range along the ground from the cloud-to-ground discharge, and is proportional to the peak current:

$$E_{100} = \frac{I_p \nu}{2\pi D \epsilon_0 c^2} \quad (15)$$

where  $D = 10^5 \text{ m}$  and  $\nu = 1.5 \times 10^8 \text{ m s}^{-1}$ .

[26] Note that this equation assumes a transmission line (TL) model for the lightning current, contradictory to our use of equations (1)–(3) for the source. This contradiction is

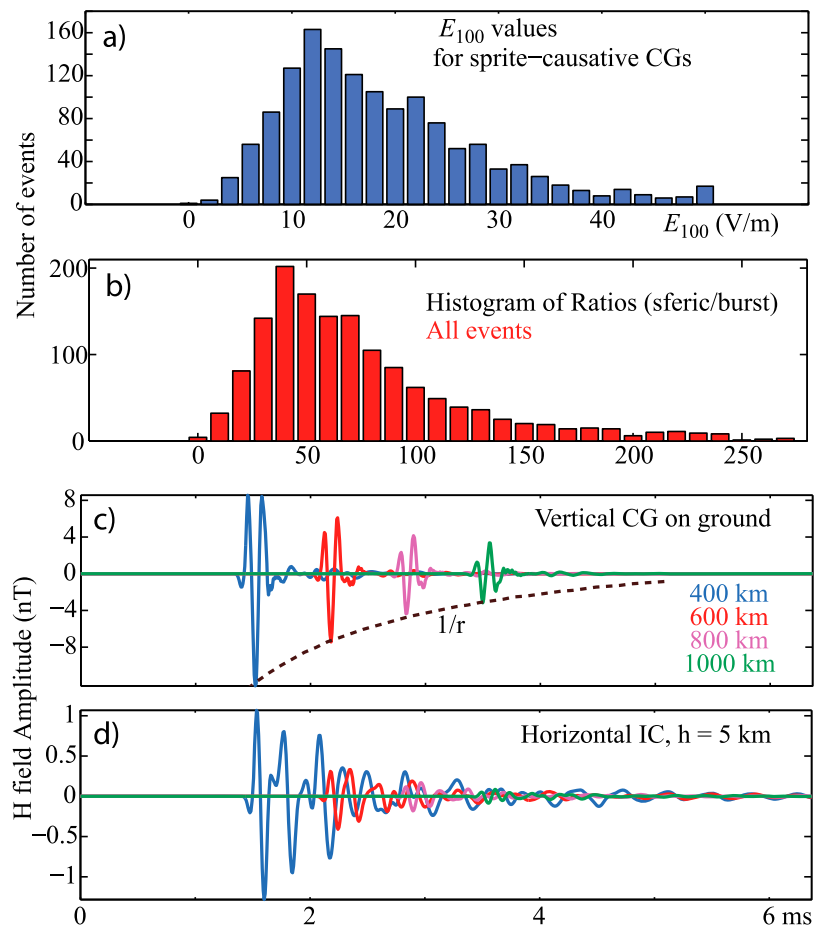


**Figure 5.** (a) Histogram of  $E_{100}$  values, directly converted from NLDN peak currents via equation (15) for sprite-causative +CGs. (b) Histogram of spheric-to-burst amplitude ratios measured in each of the events studied, including non-sprite-producing +CGs. Simulated electric field pulses received at different ranges along the ground from a 20 V/m (c) CG and (d) IC at 5 km altitude. These are used to find the expected spheric-to-burst ratio given the same source amplitude.

evident in that the radiation field in equations (1)–(3) is proportional to  $di/dt$ , while in equation (15) it is proportional to the peak current. Hence, estimates of source currents from this method for these in-cloud pulses are not reliable, and for that reason with stick to  $E_{100}^{IC}$  values, as described next.

[27] In order to simulate spider lightning and intracloud discharges with reasonable accuracy in the 3-D EMP model herein, pulse amplitudes are estimated in the following manner, as illustrated in Figure 4 for an example event. VLF broadband data recorded at Yucca Ridge Field Station (YRFS) from 1995–2000 is used with National Lightning Detection Network (NLDN) data [Cummins *et al.*, 1998] to calibrate cloud-to-ground discharges; for instance, knowing that a 90 kA peak current CG discharge corresponds to  $E_{100}^{CG} = 27 \text{ V}\cdot\text{m}^{-1}$  (equation (15)), the broadband sferic data, with NLDN-documented peak currents, can be converted to  $E_{100}^{CG}$  values. Here we are using the notation  $E_{100}^{CG}$  in the way it is defined in equation (15). The associated “sferic bursts,” which are thought to be signatures of in-cloud discharges and likely spider lightning when associated with CGs [Marshall *et al.*, 2007], are similarly converted to “ $E_{100}^{IC}$ ” amplitudes through the following three-step process.

[28] First, we compare the envelope amplitude of the sferic burst (shown in Figure 4) to that of the CG-associated sferic, after removing a noise background amplitude determined from a segment nearby (as shown in Figure 4, first panel). The distribution of these ratios is shown in Figure 5. These results show that the ratio of CG peak amplitude to sferic burst envelope amplitude varies from values close to 1 to over 200, but mostly remains in the range from 20 to 100.

[29] Second, the propagation path to the receiver is modeled to find the expected ratio of the received CG sferic amplitude to IC pulse amplitude, measured in VLF data, for pulses of the same amplitude at the source. For this purpose, an FDTD model of the Earth-ionosphere waveguide propagation is used, using a Debye-like model of the dispersive, anisotropic ionosphere [Chevalier *et al.*, 2008]. Note that this model is independent and unrelated to the EMP model described in this paper. An impulsive source of 20 V/m (i.e., a peak current of 70 kA) is input into the model, and the horizontal magnetic field ( $H_x$ ) is measured at 600, 800, and 1000 km from the source along the ground. This process is repeated for a vertical current on the ground and for a horizontal current at 5 km altitude, oriented perpendicular to the observing direction. The output is then low-pass filtered

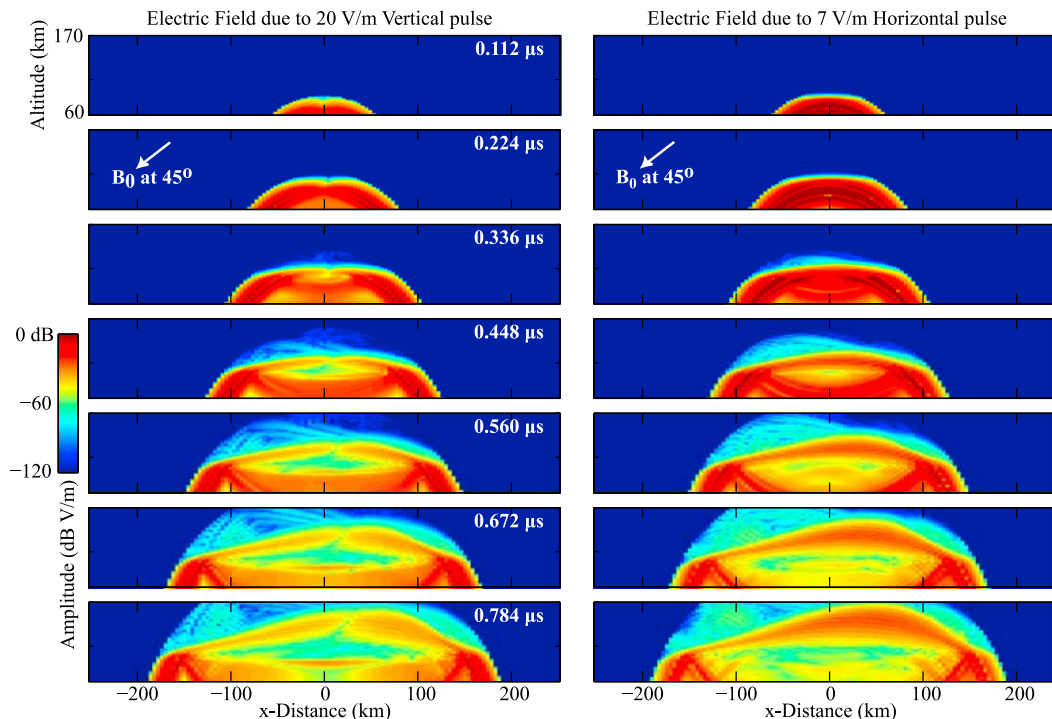


**Figure 6.** Electric field amplitudes of input vertical and horizontal pulses.

at 16 kHz to match the data used from [Marshall *et al.*, 2007]. Figures 5c and 5d show the received impulses. One can see that the amplitude of the CG decreases with distance due to  $1/r$  spreading in the first  $\sim 1000$  km (as shown by the dashed line). For the horizontal discharges, however, the amplitude drop is much faster than  $1/r$ . Horizontal impulses preferentially excite higher-order TE modes (with higher attenuation [Budden, 1961]) in the Earth-ionosphere waveguide; it is for this reason that sferic bursts are rarely observed at distances  $>1000$  km [Marshall *et al.*, 2007]. Most events studied here were in the 600–800 km range from the receiver; at those distances, the relative amplitude received for the horizontal discharge is  $\sim 10$ –30 times lower than that of the vertical CG sferic, using the impulses in Figures 5c and 5d.

[30] Third, we combine this range of values with the factor of  $\sim 20$ –100 reduction in the data amplitude of sferic bursts compared to the CG sferic (step 1), we find that the relative amplitude at the source is only 2–3 times lower for horizontal pulses in sferic bursts than for vertical discharges.

[31] This analysis is applied to each burst measured by Marshall *et al.* [2007]; i.e., the distance, CG amplitude, and sferic-to-burst ratio is taken into account for each case, and a resulting burst envelope amplitude is determined. In this way, the distribution of sferic bursts depicted in Figure 5 are found to have envelope magnitudes of  $E_{100}^{\text{IC}} \sim 5$ –10  $\text{V}\cdot\text{m}^{-1}$ . Note that this  $E_{100}^{\text{IC}}$  value is not the electric field amplitude that would be measured at 100 km lateral distance, as it is for the CG; the nomenclature used here is simply for comparison with the CG amplitudes. However, it turns out that the numerical values of  $E_{100}^{\text{IC}}$  are equivalent to the  $E_{100}^{\text{CG}}$  for the CG in terms of the source current, and the  $E_{100}^{\text{IC}}$  value reported is thus the field that would be measured 100 km in

the vertical direction, in the absence of an ionosphere and reflecting ground. These values compare well with in-cloud discharges measurements of 5–50 kA, peaking around 7 kA, by Betz *et al.* [2008], as measured in the VLF/LF range (the range 5–50 kA corresponds to  $E_{100}^{\text{IC}} = 1.5$ –15  $\text{V}\cdot\text{m}^{-1}$ ).

[32] Note that the use of a horizontal dipole oriented perpendicular to the observing direction in the model above yields an upper estimate of the field at long range, since the end-fire direction yields a null. We do not know the orientation of the observed in-cloud pulses in the data, which are likely distributed over 360 degrees. Pulses oriented parallel to the observing direction will yield smaller measurements, and so our estimates of their source amplitude will be a lower limit.

### 3. Results

#### 3.1. Single Vertical Discharge

[33] We begin by simulating vertical discharges (cloud-to-ground lightning) in order to (1) compare with previous 1-D and 2-D models and (2) determine the effect of the Earth’s magnetic field on elve geometry. Cloud-to-ground lightning is considerably better understood than in-cloud lightning, and amplitudes, stroke durations, and other parameters are generally well known, as summarized by Berger *et al.* [1975] and Rakov and Uman [2003]. Here, we use peak currents of 20–150 kA and equation (15) to find input source amplitudes in units of  $E_{100}$ .

[34] Figure 6 shows the electric field amplitude for a  $E_{100}^{\text{CG}} = 20 \text{ V}\cdot\text{m}^{-1}$  (56 kA) vertical and a  $E_{100}^{\text{IC}} = 7 \text{ V}\cdot\text{m}^{-1}$  horizontal pulse, at seven snapshots in time, as it propagates into the lower ionosphere. In this example, the Earth’s magnetic field is at 45 degree inclination as shown. The

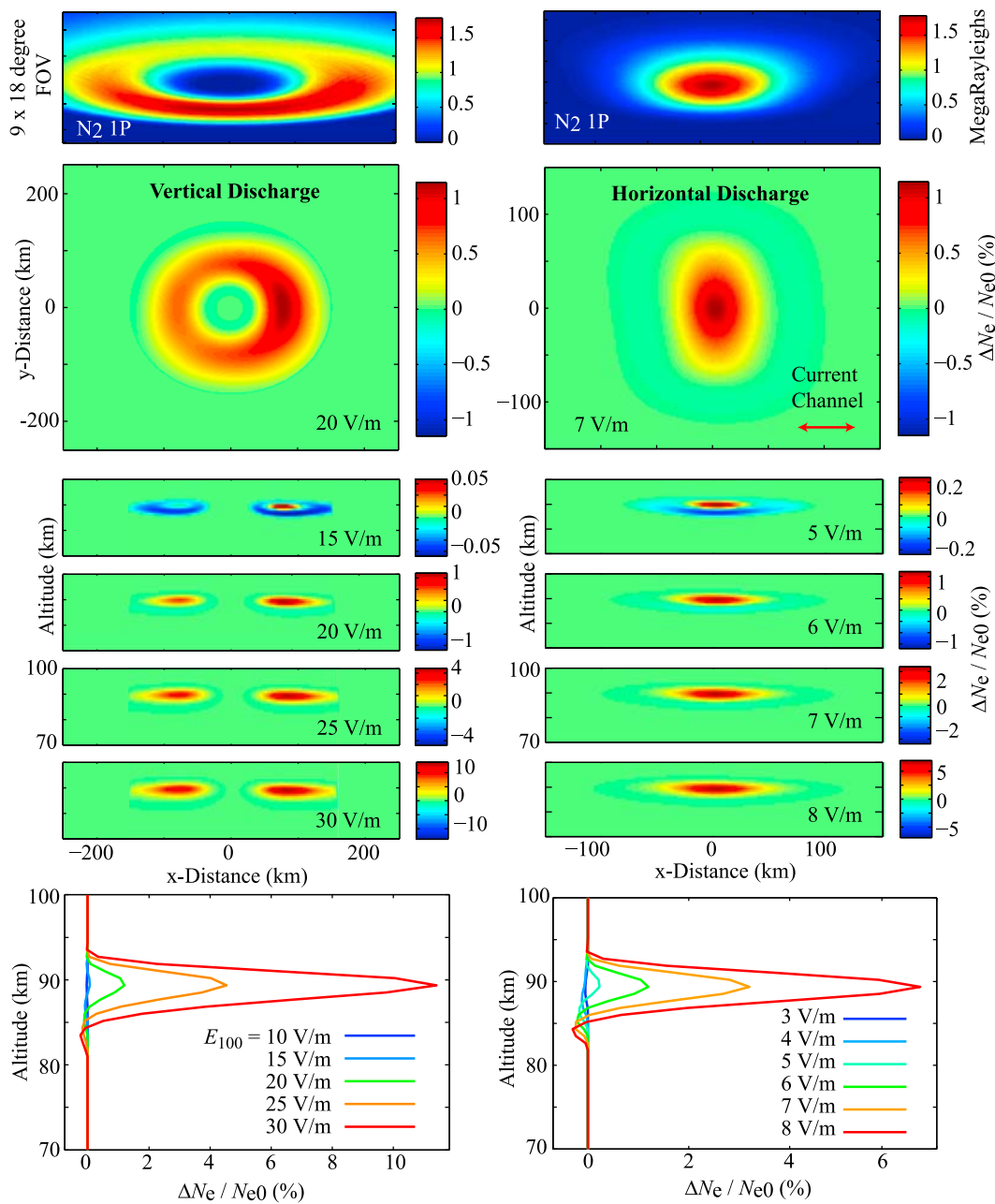


**Figure 7.** Simulations of EMP from (left) vertical discharges and (right) horizontal discharges. Shown are optical emissions viewed from a camera 400 km away on the ground; a 2-D slice in the  $x$ - $y$  plane of 3-D change in electron density; 1-D slices in the  $x$ - $z$  plane for four amplitudes; and 1-D profiles of electron density changes.

pulses start to impinge on the ionosphere in the third frame ( $t = 0.336 \mu\text{s}$ ), after which the reflection from the ionosphere is evident, with waves propagating back toward the lower boundary. Most of the fields propagate below the ionosphere in the Earth-ionosphere waveguide as expected; however, significant fields leak through the ionosphere. In the upper regions of the ionosphere, where the collision rate is much lower, the fields are in the whistler mode and tend to follow the Earth's magnetic field, creating an asymmetry in the field pattern. Further comments will be made comparing the vertical and horizontal cases in section 3.2.

[35] Because of the radiation pattern of a vertical dipole on the ground, the maximum field at 70 km altitude is only  $10.4 \text{ V}\cdot\text{m}^{-1}$ ; in this connection, the results shown here differ from previous work in one dimension, such as that of *Taranenko et al.* [1993a, 1993b], which simply injected a field amplitude at the lower boundary (70 km in their work). For this pulse we use  $1/\tau = 10^5$ , which is among the fastest return strokes for CG discharges, but within measured values [Berger et al., 1975; Rakov and Uman, 2003]. The magnetic field is taken to have a dip angle of  $45^\circ$ , corresponding to a geomagnetic latitude of  $\sim 27^\circ$ . Note that most elves observed by the ISUAL experiment onboard the

**Table 1.** Total Change in Electrons and Change in Electron Density for Simulations in Figures 7 and 13<sup>a</sup>

| Simulation Type | Amplitude (V/m) | Figure | $\Delta e$             | $\Delta N_e$ (cm <sup>-3</sup> ) |
|-----------------|-----------------|--------|------------------------|----------------------------------|
| Vertical        | 15              | 7      | $-2.43 \times 10^{19}$ | -0.07                            |
| Vertical        | 20              | 7      | $1.57 \times 10^{20}$  | 0.44                             |
| Vertical        | 25              | 7      | $1.07 \times 10^{21}$  | 3.04                             |
| Vertical        | 30              | 7      | $3.41 \times 10^{21}$  | 9.64                             |
| Vertical        | 35              |        | $7.91 \times 10^{21}$  | 22.39                            |
| Vertical        | 40              |        | $1.53 \times 10^{22}$  | 43.25                            |
| Horizontal      | 5               | 7      | $-7.82 \times 10^{18}$ | -0.03                            |
| Horizontal      | 6               | 7      | $-1.16 \times 10^{19}$ | -0.04                            |
| Horizontal      | 7               | 7      | $-1.39 \times 10^{19}$ | 0.05                             |
| Horizontal      | 8               | 7      | $1.06 \times 10^{20}$  | 0.35                             |
| Horizontal      | 9               |        | $3.13 \times 10^{20}$  | 1.04                             |
| Horizontal      | 10              |        | $6.84 \times 10^{20}$  | 2.28                             |
| 60 pulses       | 5               | 13     | $-4.70 \times 10^{20}$ | -1.57                            |
| 60 pulses       | 7               | 13     | $5.09 \times 10^{20}$  | 1.70                             |
| 60 pulses       | 10              | 13     | $1.87 \times 10^{22}$  | 62.37                            |
| 100 pulses      | random          | 13     | $7.25 \times 10^{21}$  | 24.16                            |

<sup>a</sup> $\Delta e$ , total change in electrons;  $\Delta N_e$ , change in electron density (cm<sup>-3</sup>).

FORMOSAT-2 satellite are seen in the tropics, near the equator [Mende *et al.*, 2005b] (generally following the global distribution of lightning), so that 45° is a good upper limit on the magnetic dip angle.

[36] Figure 7 (left) shows simulation results for  $\Delta N_e/N_{e_0}$ , the fractional change in electron density, for vertical dipoles of  $E_{100}^{\text{CG}} = 15, 20, 25,$  and  $30 \text{ V-m}^{-1}$ , as well as optical emissions, for the  $E_{100}^{\text{CG}} = 20 \text{ V-m}^{-1}$  case (Figure 7, left, first panel). We see that while dissociative attachment is prevalent for the  $E_{100}^{\text{CG}} = 15 \text{ V-m}^{-1}$  case, ionization takes over at  $E_{100}^{\text{CG}} = 20 \text{ V-m}^{-1}$  and quickly dominates. This result is most evident in the 1-D slices shown at bottom right. The dominance of ionization is attributed to the small window of electron energies where attachment dominates in Figure 3, with a relatively low production rate, while above  $E_k$  ionization takes over and has a considerably higher rate at high electric fields. The Earth's magnetic field causes an observable asymmetry in the electron density perturbation at  $E_{100}^{\text{CG}} = 20 \text{ V-m}^{-1}$  (Figure 7, left, first panel), but the asym-

metry is relatively small in the optical emissions (Figure 7, right, first panel).

[37] In the directions perpendicular to  $\mathbf{B}_0$  the density changes and optical emissions are strongest, since in those directions the EMP electric field is along the magnetic field (i.e.,  $\bar{E} \parallel \mathbf{B}_0$ ). As a function of the amplitude of the input pulse, the asymmetry is strongest for lower-amplitude pulses, since the “effective field” is reduced according to equation (8). This equation implies that the lower the field intensity, the greater is the asymmetry due to the magnetic field. Physically, this result makes sense since when the EMP electric field is more intense, the less important is the role of the magnetic field in facilitating (parallel direction) or inhibiting (perpendicular direction) collisions. Events that are only just above the respective thresholds of attachment, optical emissions, or ionization thus exhibit the greatest asymmetry. This result is reflected in Figure 7, where the asymmetry is much less obvious when the amplitude reaches  $E_{100}^{\text{CG}} = 30 \text{ V-m}^{-1}$ ; and for the  $E_{100}^{\text{CG}} = 20 \text{ V-m}^{-1}$  case, the asymmetry is much more prominent in ionization than it is in the optical emissions.

[38] A comment on the choice of pulse duration ( $\sim 20 \mu\text{s}$ ) is in order here. Due to the use of the second-order Mur boundary condition at the input boundary, longer pulse durations are difficult to simulate in the current version of the model. Longer pulse durations do not affect the Electric field amplitude in the ionosphere, since  $E_{100}$  and  $\tau$  are forced to be independent. Thus, a larger  $\tau$  merely extends the duration of the electric field in the ionosphere. This longer duration increases ionization, attachment, and optical emissions on an absolute scale, but their relative contributions do not change since the field amplitude is the same. Hence, the qualitative results should not be significantly affected by this choice of pulse duration  $\tau$ .

[39] Mende *et al.* [2005a] calculates a total ionization change of 210 electrons per cm<sup>3</sup> for an elve observed from the FORMOSAT-2 satellite, assuming a disturbed volume of 165 km in radius and 10 km thick. Our simulations agree very well with this volume estimate for the vertical CG; the

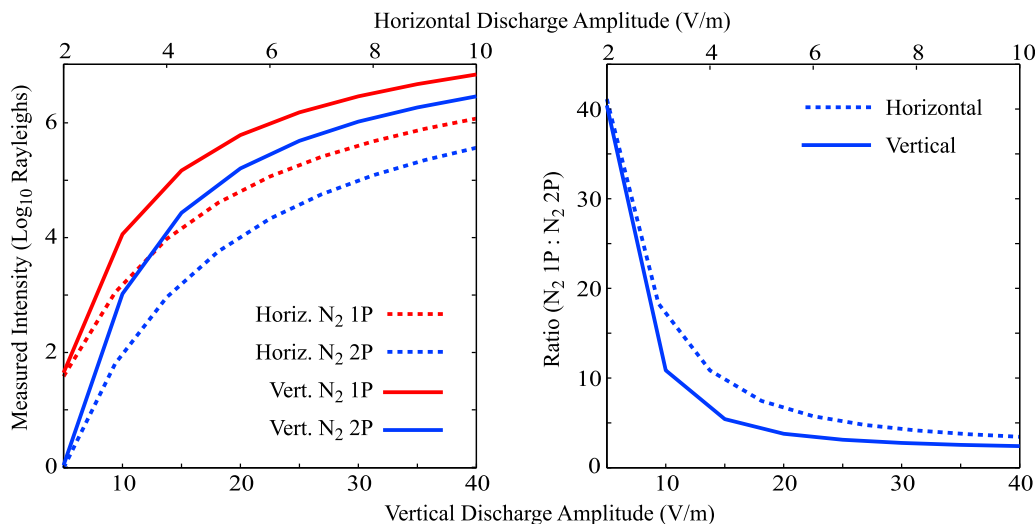


**Figure 8.** (left) Optical intensities for the N<sub>2</sub> 1P and 2P band systems for horizontal pulses from 2–10 V-m<sup>-1</sup> and vertical pulses from 5–40 V-m<sup>-1</sup>. (right) Ratio of intensities in 1P and 2P for the same pulses.

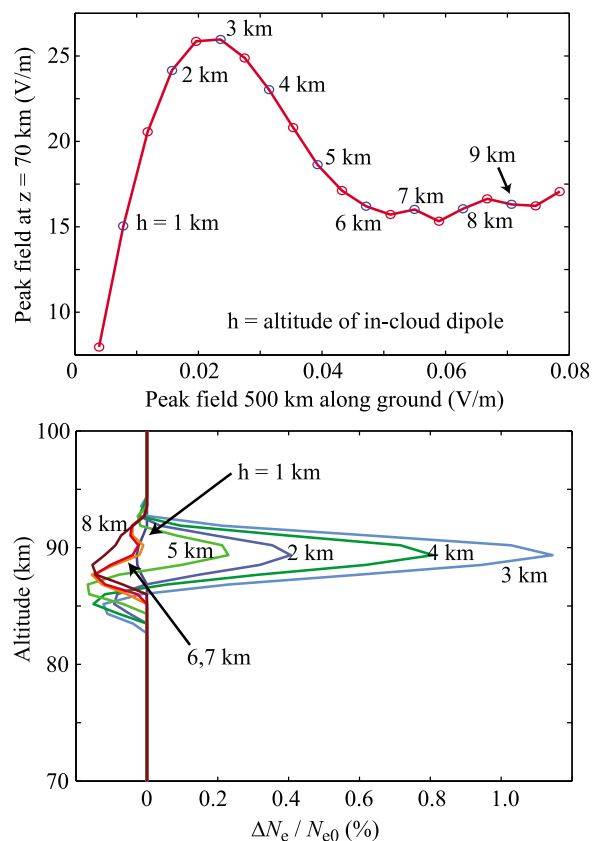


**Figure 9.** Effect of variation in the dipole altitude. (top) Analytical calculations of the field amplitude at 70 km altitude above the discharge versus the observed amplitude along the ground at 500 km. See the text for a full discussion. (bottom) Simulation results for discharges at 1–8 km altitude.

disturbed region in Figure 7 has a radius of about 155 km and a thickness of about 6 km in altitude. Using this approximate volume, and  $200 \times 300 \times 6$  km for the horizontal cases (Figure 7, right), we find the average electron density changes shown in Table 1 for the results in Figures 7 and 13. For the case studied by *Mende et al.* [2005a], an average reduced electric field of 200 Td ( $200 \times 10^{-17}$  V-cm<sup>2</sup>) is derived over the volume disturbed; at 90 km this corresponds to an average field of 12.5 V/m. For our simulations an input pulse of  $E_{100} = 35$  V/m gives this average; thus our calculated electron density change (fifth row of Table 1; about 22 electrons per cm<sup>3</sup>) is within about an order of magnitude. However, comparing our use of a  $\sim 20$   $\mu$ s pulse to a more realistic  $\sim 100$ – $200$   $\mu$ s pulse, the cumulative effects bring our numbers very close to the 210 electrons per cm<sup>3</sup> measured by *Mende et al.* [2005a]. Future updates to the model will allow us to simulate these longer pulses and make more accurate comparisons.

### 3.2. Horizontal Discharge

[40] The 3-D nature of this model allows us to realistically simulate horizontal discharges for the first time. Figure 6 (right) shows the electric field amplitudes at various snapshots in time for a  $E_{100}^{\text{IC}} = 7$  V-m<sup>-1</sup> horizontal pulse at 5 km altitude. This pulse has the same duration (20  $\mu$ s) as the

vertical  $E_{100}^{\text{CG}} = 20$  V-m<sup>-1</sup> pulse in Figure 6 (left). First, note that for the horizontal case, there is no null in the vertical direction, as expected. Second, there is much less intensity at late times at altitudes in the 70–90 km range; in the vertical case, these persistent fields are due to the  $1/r^3$  terms in equations (1) and (2) related to  $M$ , the integral of the dipole moment. Otherwise, the field patterns look very similar to the vertical case.

[41] Figure 7 (right) shows density changes and optical emissions for this  $E_{100}^{\text{IC}} = 7$  V-m<sup>-1</sup> pulse at 5 km altitude, with a pulse duration of  $\tau = 20$   $\mu$ s. Note that the electron density changes for this  $E_{100}^{\text{IC}} = 7$  V-m<sup>-1</sup> discharge compare to the effects of a  $E_{100}^{\text{CG}} = 20$  V-m<sup>-1</sup> CG for both magnitude and the relative contributions of ionization and attachment. However, the shape of the disturbed region is significantly different, and the total volume disturbed is somewhat smaller (note the different  $x$  and  $y$  scales). The absence of the ring shape is simply due to the radiation pattern of the CG versus IC discharges; where the CG discharge had a null in the vertical direction, the IC discharge has a maximum.

[42] Figure 7 (right, third through sixth panels) shows results for horizontal discharges as a function of the input amplitude. Again, note that much smaller pulses create effects with similar magnitude compared to vertical discharges of the same  $E_{100}$ ; for example, ionization begins around  $E_{100}^{\text{IC}} = 5$  V-m<sup>-1</sup>, whereas for the vertical discharge,  $E_{100}^{\text{CG}} = 15$  V-m<sup>-1</sup> is required. The lowered threshold is of course due to (1) the radiation pattern of the horizontal discharge, having its maximum in the vertical direction; (2) the difference in distance, since the greatest effects of the vertical discharge are seen  $\sim 80$  km away laterally from the discharge; and (3) the reflection from the conducting ground, which in these simulations is treated as a perfect conductor. The combined effects of these three factors also account for the three-times lower amplitude required in Figure 7 to achieve effects similar to the CG case.

[43] Results shown here are once again for  $1/\tau = 10^5$  s<sup>-1</sup>, or a  $\sim 20$   $\mu$ s pulse. Measurements of in-cloud lightning activity from *Proctor et al.* [1988] and *Mazur et al.* [1997] report on intracloud pulses of two types: 1  $\mu$ s “pulses” and “Q-trains,” bursts of pulsed activity lasting from 10 to over 400  $\mu$ s, with a median of 80  $\mu$ s [*Proctor et al.*, 1988]. Statistics are not given on the duration of individual pulses within Q-trains, as they are indistinguishable from one another. By contrast, narrow bipolar pulses (NBPs) have been reported with durations from 10 to 75  $\mu$ s [*Rakov and Uman*, 2003, Table 9.3]. However, those measurements were made in the VHF band, whose source characteristics may differ significantly from what is measured in VLF. *Smith et al.* [1999] report pulse durations for NBPs of 2.8  $\mu$ s and 26  $\mu$ s, respectively, in VHF and VLF-LF bands, the latter of which agrees well with our input pulse duration of  $\sim 20$   $\mu$ s. Statistics for pulses within so-called “spider lightning,” thought to be the source of continuing current and thus large charge moment changes in sprite-producing lightning *Stanley et al.* [1999], are not available in the literature; unfortunately, spider lightning is of the greatest interest to the current problem. For the results shown in this work,  $\sim 20$   $\mu$ s has been chosen as a mean value for three reasons: first, it falls within the range of the data described above; second, faster pulses cannot be accurately simulated with the attachment and ionization cross sections used, since

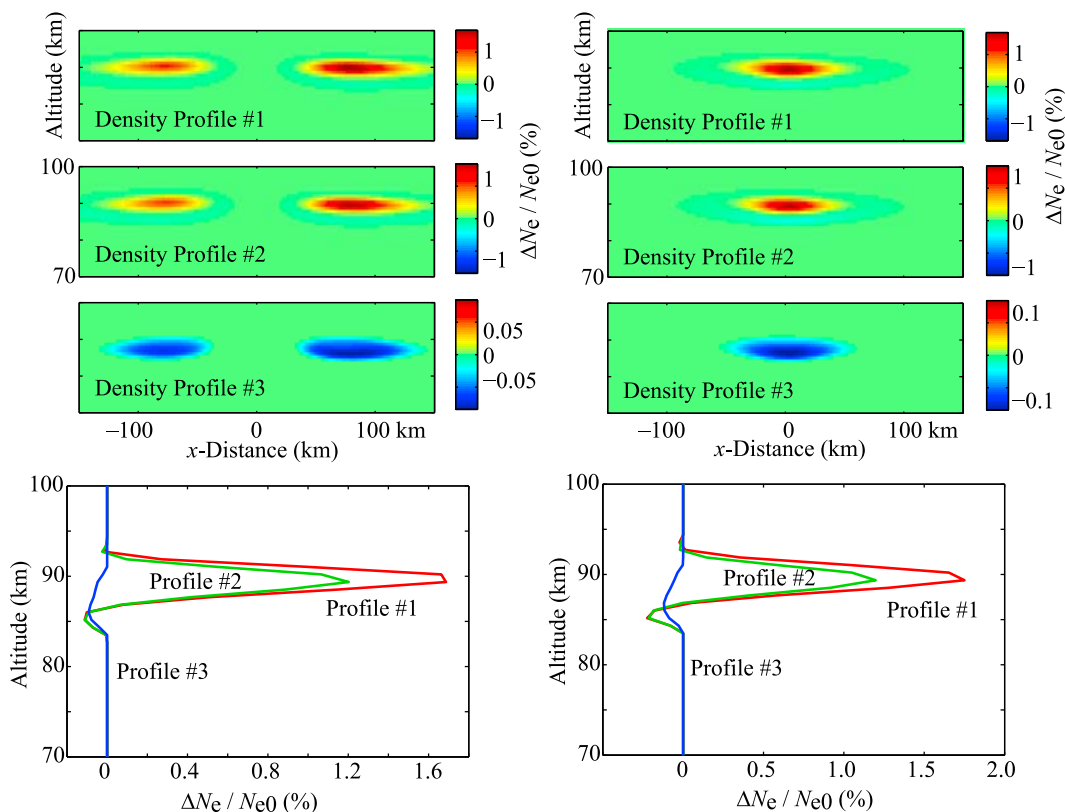


**Figure 10.** Variation with the ionospheric density profile. The dense ionosphere #3 has the weakest response in both electron density change and optical emissions.

they assume the establishment of a stationary electron distribution function over a time on the order of  $\sim 2 \mu\text{s}$  [Taranenko *et al.*, 1993a; Glukhov and Inan, 1996]; and third, slower pulses create near-field effects (the  $1/r^3$  terms in equations (1) and (2)) in the ionosphere which are not likely to exist in the fast pulses and Q-trains described by Proctor *et al.* [1988]. Furthermore, those near-field or electrostatic components would be extinguished rapidly, in about  $1 \mu\text{s}$  [Pasko *et al.*, 1997], a process that our model cannot take into account. Hence, those effects must be suppressed through the choice of pulse duration.

[44] Optical emissions from the  $E_{100}^{\text{IC}} = 7 \text{ V}\cdot\text{m}^{-1}$  pulse are also shown in Figure 7 (top right). For the same pulse duration, the optical emissions in the  $\text{N}_2$  1P and 2P band systems are very similar in magnitude to the CG results. However, it is important to note that the optical intensity for the vertical case in Figure 7 is likely to be an underestimate. As mentioned earlier, the shape and type of density perturbations (ionization versus attachment) and optical emissions are primarily controlled by the field amplitude, radiation pattern, and ionospheric profile; however, the depth of the density perturbation and intensity of the optical emissions are also controlled by the pulse duration. Longer pulse durations (larger  $\tau$ ) yield fields of shorter duration in the ionosphere. Since the ionization, attachment, and optical effects are integrated in time, slower pulses of the same  $E_{100}$  have stronger effects. The  $\sim 20 \mu\text{s}$  pulses are probably above average for horizontal pulses, but are on the low end for vertical CG discharges; hence, those effects would in fact be enhanced in the case of the true pulse duration. For a pulse

of  $\sim 100 \mu\text{s}$ , for example, one can expect optical emissions to have a similar shape but  $\sim 5$  times higher intensity. This estimate has been confirmed by simulations that are not shown here.

[45] Figure 8 (left) shows the intensities of optical emissions, integrated over the field of view, versus vertical and horizontal pulse amplitudes, for the  $\text{N}_2$  1P and 2P band systems. Figure 8 (left) shows that the intensities vary in a predictable way with amplitude; furthermore, this variation is independent of the pulse duration. Figure 8 (right) shows the ratio of  $\text{N}_2$  1P to  $\text{N}_2$  2P intensities versus pulse amplitude; these ratios are similarly independent of pulse duration. Using these results, the discharge amplitudes can be inferred from ground or space-based measurements of elves.

### 3.3. Parameter Variations for Horizontal Discharges

[46] In this section, the parameters for horizontal discharges are varied, including altitude, dipole orientation, magnetic field dip angle, and ionospheric density profile, in order to quantify the effects of these inputs on the resulting density changes.

#### 3.3.1. Altitudes of IC Discharges

[47] Proctor [1991] presents data on the origin heights of IC and CG discharges, ranging primarily from 2–10 km. Mazur *et al.* [1997] provides an overview of source pulse altitudes of IC discharges measured with time-of-arrival (TOA) versus interferometric (ITF) receiver systems. Results therein show that TOA-received sources, which are preferentially single, fast  $\sim 1 \mu\text{s}$  pulses, range in altitude from 5–15 km with a peak in the distribution at  $\sim 10$  km,

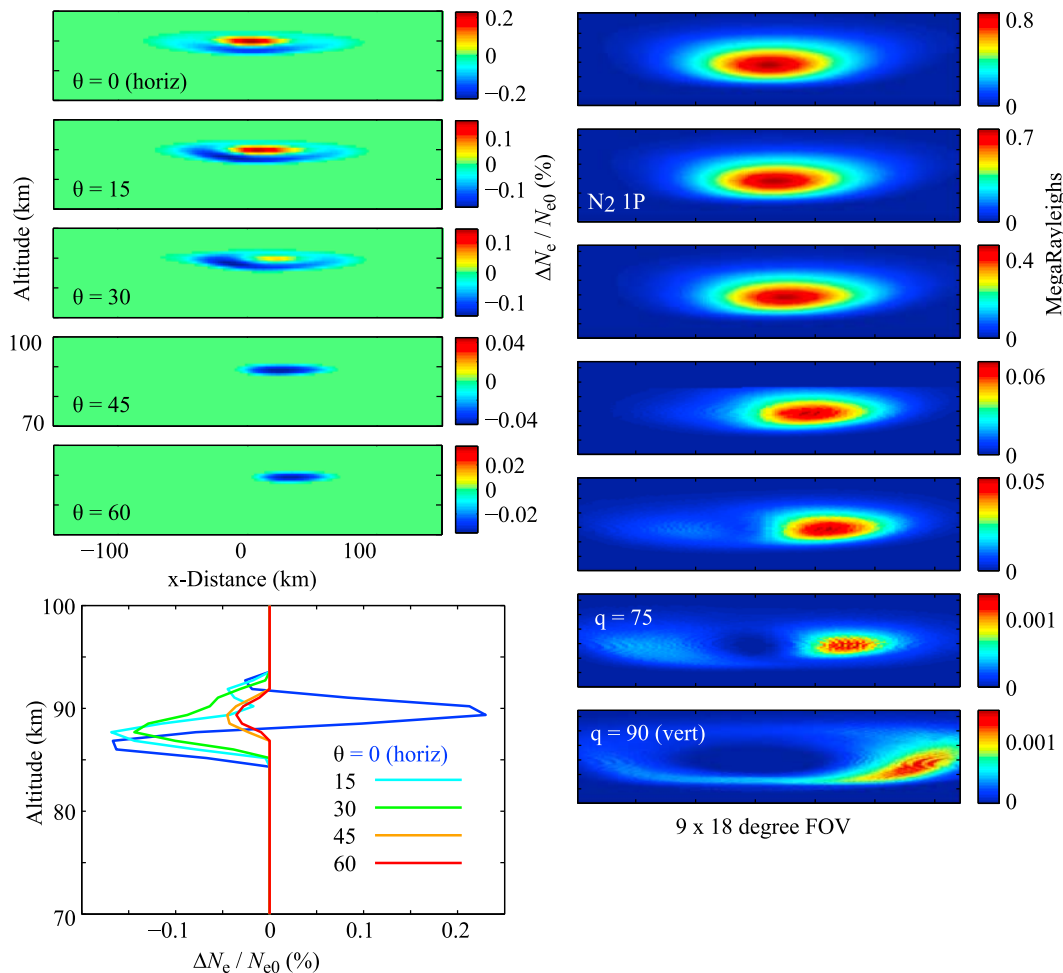


**Figure 11.** Variation in horizontal dipole orientation angle for pulses of  $5 \text{ V}\cdot\text{m}^{-1}$  at 5 km altitude, with  $B_0$  at 45 degrees.

whereas ITF sources, which are preferentially the longer Q-trains of *Proctor et al.* [1988], range in altitude from 1–10 km, with a peak in the distribution at  $\sim 5$  km. *Marshall et al.* [2007] discussed these results and concluded that the latter category may constitute the currents in spider lightning, which is reported to have altitudes of 4–6 km [Stanley et al., 1999; Mazur et al., 1998]. Similarly, *Noble et al.* [2004] reports on discharges observed by the New Mexico Tech Lightning Mapping Array (LMA) with altitudes from 1–12 km, while *Thomas et al.* [2000] shows 5–7 km altitudes for “hybrid IC-CG discharges,” those IC pulses associated with a CG. These discharge altitudes are used in the present work, and most results herein are for a discharge altitude of 5 km, with variations shown below.

[48] Figure 9 (top) shows results of analytical calculations using equations (1)–(3), using a  $10 \text{ V}\cdot\text{m}^{-1}$  horizontal source input, of the maximum field amplitude at 70 km altitude, versus the amplitude along the ground at 500 km range, for a range of dipole altitudes from 0.5–10 km. These calculations are for  $1/\tau = 10^5 \text{ s}^{-1}$ , neglect the effect of the ionosphere, and predict that the field has its highest magnitude for pulses at 3 km, and that the amplitude slowly drops off up to 6 km altitude. This result is due to the ground reflection: for a source altitude of 3 km, the ground reflection interferes constructively with the input pulse; below and

above 3 km, the interference becomes more and more destructive. At its point of most constructive interference (at 3 km source altitude), the fields measured are essentially double the input field, showing that the ground reflection plays a vital role in ionospheric effects (Note that  $1/\tau = 10^5 \text{ s}^{-1}$  corresponds to a spatial pulse width of about 6 km). It is important to note that this optimal altitude varies depending on the pulse frequency content (i.e., the pulse duration, given by  $\tau$ ). Note that a source pulse at 3 km altitude also has the highest “efficiency” in terms of directly affecting the ionosphere: it produces a strong field in the ionosphere but a very small amplitude 500 km away on the ground, where a VLF receiver might be located. While these calculations are simply for the electric field magnitude, we use them here as a “prediction” of the ionospheric effect of pulses at different altitudes.

[49] Figure 9 (bottom) shows results from simulations with dipoles located at different altitudes, to demonstrate the effects described above. These results agree with the predictions in Figure 9 (top); the largest perturbations are seen for a source dipole at 3 km, with effects diminishing as the source altitude is increased or decreased. For a source altitude above 5 km, the maximum density change does not vary greatly with source altitude, in agreement with the electric field calculations; essentially, for higher source

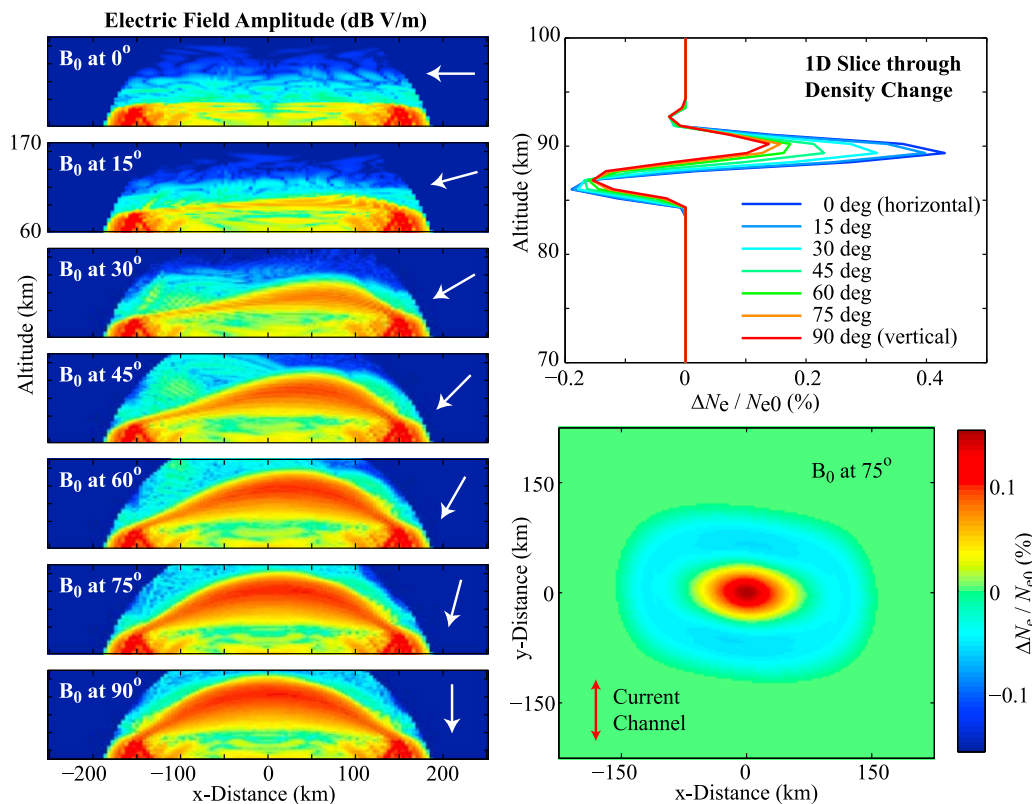


**Figure 12.** Variation in magnetic field dip angle for horizontal pulses of  $7 \text{ V}\cdot\text{m}^{-1}$  at 5 km altitude.

altitudes the primary pulse and its ground reflection become separated in time and do not interfere, so that the effects are those of two successive impulses.

### 3.3.2. Ionospheric Profiles

[50] As shown in previous work [Taranenko *et al.*, 1993a; Barrington-Leigh *et al.*, 2001], the choice of ionospheric profile has a very significant effect on the electron density changes and optical emissions. We show the results of a  $E_{100}^{\text{CG}} = 20 \text{ V}\cdot\text{m}^{-1}$  vertical discharge (Figure 10, left) and a  $E_{100}^{\text{IC}} = 7 \text{ V}\cdot\text{m}^{-1}$  horizontal dipole at 5 km altitude (Figure 10, right), incident on three different electron density profiles. Density profile #2 is used in all other results shown in this paper. Profile #1 is slightly more tenuous than #2, and shows a slight increase in the ionospheric effects, both in density changes and optical emissions. Profile #3, a dense nighttime profile, tends to suppress the effects of the input pulse compared to #2, and shows only effects of attachment. This result is in agreement with Taranenko *et al.* [1993a]; therein, the authors had to increase the input pulse from  $E_{100}^{\text{CG}} = 20 \text{ V}\cdot\text{m}^{-1}$  to  $35 \text{ V}\cdot\text{m}^{-1}$  in order to see similar effects for a denser ambient profile. Generally, as described by Taranenko *et al.* [1993a], effects of CG and IC pulses are relatively small in dense nighttime or daytime ionospheric conditions, and are furthermore relatively less important, and probably not measurable, given the much larger background density. At nighttime, such a circumstance may occur, for instance, after a large lightning-induced electron precipitation (LEP) event [Peter and Inan, 2005; Peter *et al.*, 2006]. The large density increases associated with such events, which may cover a large spatial area, may act to

suppress ionospheric effects of lightning discharges (e.g., production of elves) below the affected region.

### 3.3.3. Dipole Orientation

[51] While we have assumed “in-cloud lightning” to be synonymous with “horizontal” lightning, in-cloud lightning discharges may occur with any orientation. In fact, in many cases the discharge occurs between two reservoirs of opposite-polarity charge that are vertically separated, as in the work of Krehbiel *et al.* [2008]. In the case of spider lightning, which extends out many tens of km into the stratiform region of large thunderstorms [Lyons *et al.*, 1998], the discharge may be predominantly horizontal.

[52] Figure 11 shows results for a  $E_{100}^{\text{IC}} = 5 \text{ V}\cdot\text{m}^{-1}$  pulse at 5 km altitude with a duration of  $20 \mu\text{s}$ , with the dipole angle varied from 0 degrees (horizontal) to 90 degrees (vertical). In all cases the dipole is oriented so that the projection onto the ground is parallel to that of the Earth’s magnetic field  $B_0$ ; i.e., both are in the  $y$ - $z$  plane. As expected, the resulting electron density change decreases rapidly as the dipole varies away from horizontal. The radiation pattern of a dipole is maximum perpendicular to the current, so sources at angles off horizontal have maxima in the pattern away from vertical. Furthermore, the interference with the ground reflection is significantly affected by the radiation pattern. Above 60 degrees, there is no change in electron density for this  $E_{100}^{\text{IC}} = 5 \text{ V}\cdot\text{m}^{-1}$  pulse. The optical emissions show a similar effect, with rapidly decreasing intensity with dipole angle toward vertical. The vertical dipole, in fact, has an elve-like shape, due to the null in the radiation pattern, but its intensity is far below observable.

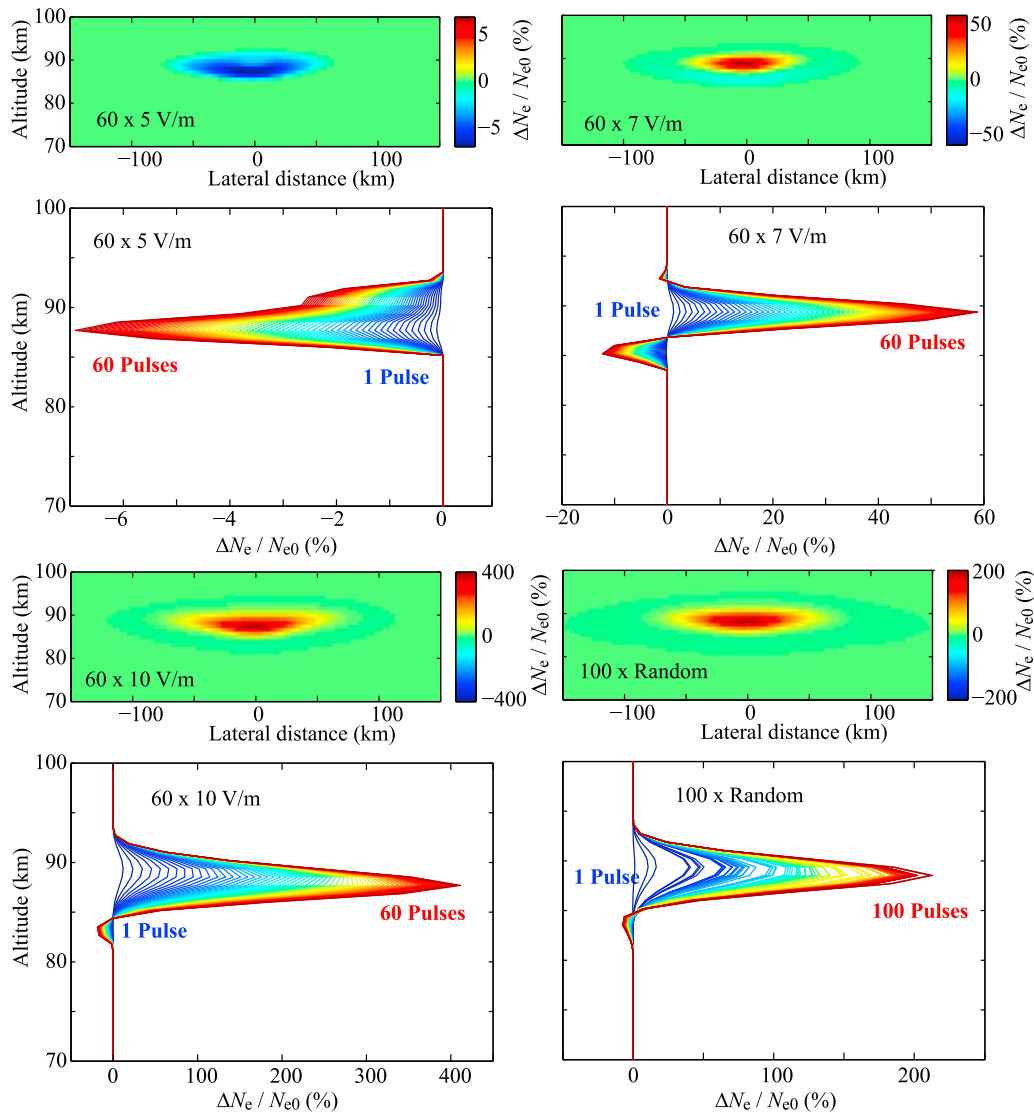


**Figure 13.** Effects of multiple pulses on the ionosphere. Note that optical emissions are the same as for each pulse separately, since the optical relaxation times are short compared to the interpulse timing.

### 3.3.4. Magnetic Field Orientation

[53] Variation in the orientation of the Earth’s magnetic field is (partially) equivalent to variation in latitude. A horizontal magnetic field occurs at the magnetic equator; low angles correspond to the tropics; and higher angles correspond to high latitudes. The vast majority of lightning occurs over land and at lower latitudes, with very little over 50 degrees geographic latitude [e.g., *Christian et al.*, 2003, Figure 4]. Figure 12 shows results wherein the Earth’s magnetic field orientation has been varied from horizontal (i.e., at the magnetic equator) to vertical (at the magnetic poles). Note that this variation is not quite equivalent to a variation in latitude; we have not changed the magnetic field amplitude from its value of 50,000 nT, which corresponds to the value at 37°N, 100°E, in Kansas, near where much of the data of *Marshall et al.* [2007] was taken.

[54] Figure 12 (left) shows the electric field amplitudes at  $t = 0.784 \mu\text{s}$ , measured from the time the pulse reaches 70 km altitude, for each of the magnetic field angles. Note that when  $\mathbf{B}_0$  is horizontal, as in Figure 12 (top left), the

magnetic field “shields” the higher altitudes, preventing the fields from penetrating into the magnetosphere. This behavior is explained by the angular dependence of the imaginary part of the refractive index. However, as the magnetic field angle is increased, fields do manage to penetrate through the ionosphere to higher altitudes. For this reason, VLF signatures of lightning (known on the ground as sferics but in space as so-called “0+ whistlers”) are less likely to be seen on satellites near the equator compared to higher latitudes.

[55] Furthermore, we see that a horizontal  $\mathbf{B}_0$  results in higher density changes, by about a factor of two compared to the vertical  $\mathbf{B}_0$ . The horizontal  $\mathbf{B}_0$  results in a stronger reflection from the ionosphere (since fields do not penetrate into the magnetosphere); this reflection thus has a stronger constructive interference with the upgoing pulse, resulting in higher fields and stronger effects. Note that the Earth’s magnetic field is about a factor of two stronger at the magnetic poles than it is at the equator; hence, this effect

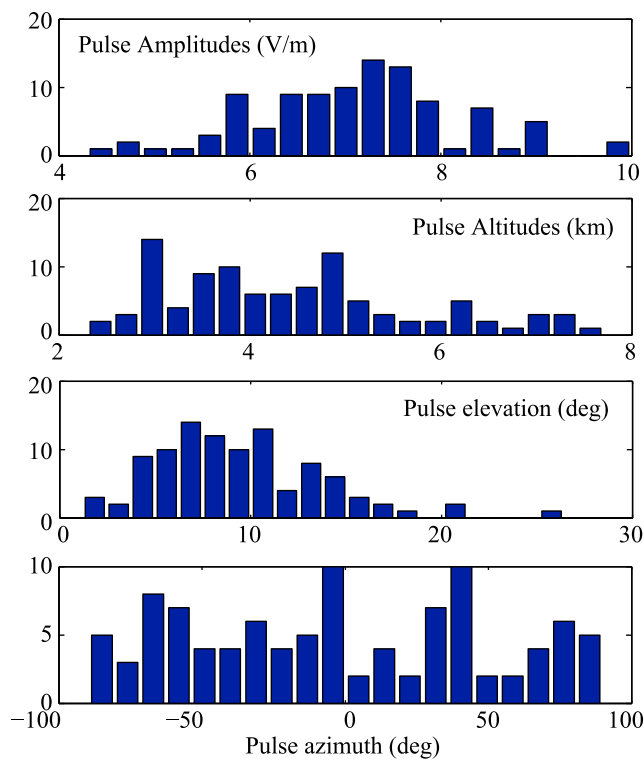


**Figure 14.** Parameters of pulses for random sequence in Figure 13.

should be somewhat reduced by the variation of the Earth’s magnetic field intensity.

### 3.4. Repeated Pulses

[56] As shown by *Taranenko* [1993], successive pulses may have a cumulative effect on density changes in the ionosphere, yielding density perturbations that may be measurable with subionospheric VLF transmitter signals [*Inan et al.*, 1995; *Johnson et al.*, 1999]. Sprite-producing lightning events, as well as many other lightning events, often have a large component of in-cloud lightning [*Marshall et al.*, 2007], and in the case of sprites this may be so-called spider lightning [*Stanley et al.*, 1999]. It is thus important to model the effect of multiple in-cloud horizontal impulses on the lower ionosphere. In fact, very rarely do in-cloud discharges consist of single events, but rather many tens [*Villanueva et al.*, 1994] or even hundreds of impulsive discharges [see, e.g., *Mazur et al.*, 1997; *Noble et al.*, 2004], except maybe in the case of narrow bipolar discharges [*Smith et al.*, 1999].

[57] The effect of multiple pulses is modeled by using the resulting 3-D electron density profile from one run of the simulation as the input density profile for a subsequent run. This process can then be streamlined and run iteratively for any reasonable number of pulses (limited only by computer time). Note that the relaxation time of newly introduced ionization at 80–100 km altitudes is about  $\sim 10$ – $100$  s [*Pasko and Inan*, 1994], while in-cloud lightning bursts last no longer than  $\sim 3$  s; as such, the relaxation process can be ignored. Ignoring the pair of plots in Figure 13 (bottom right) for the moment, Figure 13 shows the effects of up to 60 horizontal discharge pulses of  $E_{100}^{\text{IC}} = 5, 7$  and  $10 \text{ V}\cdot\text{m}^{-1}$ .

The optical output for each pulse is very nearly the same as for a single pulse, with small variations due to the change in electron density; the  $\text{N}_2$  optical emissions have short lifetimes ( $\sim 10$ – $100$  ns) compared to the realistic interpulse period ( $\sim \mu\text{s}$ ), and so is taken to have extinguished before the next pulse; high-speed photometry should thus see a sequence of independent, repeated pulses with intensities as measured in Figure 7. In these first three sets of simulations the amplitudes and discharge directions have been kept constant for simplicity.

[58] Results show that for 60 pulses, a significant density change accumulates in the lower ionosphere, which initially increases the 3-D electron density perturbation cumulatively, very nearly linearly with number of pulses. This linear trend must of course break down for the negative part of the perturbation when it reaches many tens of percent, as in equation (11) the rate of change of electron density  $dN_e/dt$  depends on  $N_e$  itself. The possibility that these multipulse density perturbations could be measured by VLF transmitter signals is explored by *Marshall et al.* [2008].

[59] The fourth set of simulations in Figure 13 (bottom right) show results for 100 successive pulses, where each pulse is given a random altitude, amplitude, and orientation in three dimensions. These parameters are taken from realistic values and their statistics are shown in the histograms in Figure 14. This sequence thus represents the closest approximation to the ionospheric effects of a “real” in-cloud burst. With most of the pulse amplitudes falling in the  $E_{100}^{\text{IC}} = 6$ – $8 \text{ V}\cdot\text{m}^{-1}$  range, this sequence of 100 pulses yields a density increase of over 200%.

## 4. Summary

[60] The results of this paper can be summarized as follows:

[61] 1. For realistic CG lightning amplitudes above about 56 kA ( $E_{100}^{\text{CG}} = 15 \text{ V}\cdot\text{m}^{-1}$ ), the threshold for ionization is easily reached, so that most EMPs result in a dramatic increase in the local electron density. For amplitudes below  $15 \text{ V}\cdot\text{m}^{-1}$ , attachment causes a reduction in electron density, but the total effect is very small. As mentioned in the introduction, a prior 3-D model of the EMP-ionosphere interaction was presented by *Cho and Rycroft* [2001]. In that work, while attachment was mentioned and may have been included in the model calculations, the presented results do not show the effects of attachment.

[62] 2. Intense horizontal impulses, either in-cloud discharges, narrow bipolar pulses, or spider lightning, may create significant density perturbations in the overlying ionosphere as well as detectable optical emissions.

[63] 3. The parameters of the in-cloud discharge (altitude, amplitude, duration, and orientation) as well as the ionospheric density and magnetic field  $B_0$  have a significant effect on the EMP-ionosphere interaction. Furthermore, the effects are interdependent; for example, there is a maximum field for a dipole at a particular altitude, but that altitude is strongly dependent on the duration. For this reason there is not a particular altitude, duration, or orientation that is the “best.”

[64] 4. A sequence of many IC discharges, as in most IC and spider lightning events, may create a cumulative density perturbation in the overlying ionosphere of many tens to

hundreds of percent density change. *Marshall et al.* [2008] further showed that these multipulse density perturbations may be detectable as Early VLF events, and that Early VLF events may in fact be the signature of these ionospheric disturbances.

[65] Point number two above has a further implication: each of these sequences of pulses creates a potentially observable optical event as shown in Figures 7 (top left) and 7 (top right), and so the sequence of pulses should create a sequence of “flashing elves” in the ionosphere. These are likely too dim to be observed by ground cameras, but could potentially be observed by ground photometer instruments or satellites.

[66] **Acknowledgments.** This work was supported by Office of Naval Research grant N00014-03-1-0333 and National Science Foundation grant ATM-0551174. Robert Marshall is supported by a Stanford Lieberman Fellowship.

[67] Zuyin Pu thanks the reviewers for their assistance in evaluating this paper.

## References

- Aleksandrov, N. L., A. E. Bazelyan, E. M. Bazelyan, and I. V. Kochetov (1995), Modeling of long streamers in atmospheric-pressure air, *Plasma Phys. Rep.*, *21*(1), 60–80.
- Barrington-Leigh, C. P., U. S. Inan, M. Stanley, and S. A. Cummer (1999), Sprites triggered by negative lightning discharges, *Geophys. Res. Lett.*, *26*(24), 3605–3608.
- Barrington-Leigh, C. P., U. S. Inan, and M. Stanley (2001), Identification of sprite and elves with intensified video and broadband array photometry, *J. Geophys. Res.*, *106*(A2), 1741–1750.
- Berger, K., R. B. Anderson, and H. Kroninger (1975), Parameters of lightning flashes, *Electra*, *80*, 223–237.
- Betz, H. D., T. C. Marshall, M. Stolzenburg, K. Schmidt, W. P. Oettinger, E. Defer, J. Konarski, P. Laroche, and F. Dombai (2008), Detection of in-cloud lightning with VLF/LF and VHF networks for studies of the initial discharge phase, *Geophys. Res. Lett.*, *35*, L23802, doi:10.1029/2008GL035820.
- Boeck, W. L., O. H. Vaughan, R. Blakeslee, B. Vonnegut, and M. Brook (1992), Lightning induced brightening in the airglow layer, *Geophys. Res. Lett.*, *19*, 99–102.
- Budden, K. G. (1961), *The Wave-Guide Mode Theory of Wave Propagation*, Prentice-Hall, Englewood Cliffs, N. J.
- Buneman, O. (1993), TRISTAN: The 3D electromagnetic particle code, in *Computer Space Plasma Physics: Simulation Techniques and Software*, chap. 3, pp. 67–84, Terra Sci., Tokyo.
- Chevalier, T. W., U. S. Inan, and T. F. Bell (2008), Terminal impedance and antenna current distribution of a VLF electric dipole in the inner magnetosphere, *IEEE Trans. Antennas Propag.*, *56*(8), 2454–2468.
- Cho, M., and M. J. Rycroft (2001), Non-uniform ionisation of the upper atmosphere due to the electromagnetic pulse from a horizontal lightning discharge, *J. Atmos. Sol. Terr. Phys.*, *63*, 559–580.
- Christian, H. J. et al. (2003), Global frequency and distribution of lightning as observed from space by the Optical Transient Detector, *J. Geophys. Res.*, *108*(D1), 4005, doi:10.1029/2002JD002347.
- Cummins, K. L., E. P. Krider, and M. D. Malone (1998), The US national lightning detection network™ and applications of cloud-to-ground lightning data by electric power utilities, *IEEE Trans. Electromagn. Compat.*, *40*, 465–480, doi:10.1109/15.736207.
- Davies, D. K. (1983), Measurements of swarm parameters in dry air, *Theor. Notes* 346, Westinghouse Electr., New York.
- Fukunishi, H., Y. Takahashi, M. Kubota, K. Sakanoi, U. S. Inan, and W. A. Lyons (1996), Elves: Lightning-induced transient luminous events in the lower ionosphere, *Geophys. Res. Lett.*, *23*, 2157–2160, doi:10.1029/96GL01979.
- Glukhov, V. S., and U. S. Inan (1996), Particle simulation of the time-dependent interaction with the ionosphere of rapidly varying lightning EMP, *Geophys. Res. Lett.*, *23*(16), 2193–2196.
- Gurevich, A. V. (1978), *Nonlinear Phenomena in the Ionosphere*, Springer-Verlag, Berlin.
- Hu, W., S. A. Cummer, and W. A. Lyons (2007), Testing sprite initiation theory using lightning measurements and modeled EM fields, *J. Geophys. Res.*, *112*, D13115, doi:10.1029/2006JD007939.
- Inan, U. S., T. F. Bell, and J. V. Rodriguez (1991), Heating and ionization of the lower ionosphere by lightning, *Geophys. Res. Lett.*, *18*(4), 705–708.
- Inan, U. S., T. F. Bell, V. P. Pasko, D. D. Sentman, E. M. Wescott, and W. A. Lyons (1995), VLF signatures of ionospheric disturbances associated with sprites, *Geophys. Res. Lett.*, *22*(24), 3461–3464.
- Inan, U. S., W. A. Sampson, and Y. N. Taranenko (1996), Space-time structure of optical flashes and ionization changes produced by lightning-EMP, *Geophys. Res. Lett.*, *23*(2), 133–136.
- Johnson, M. P., U. S. Inan, S. J. Lev-Tov, and T. F. Bell (1999), Scattering pattern of lightning-induced ionospheric disturbances associated with early/fast VLF events, *Geophys. Res. Lett.*, *26*(15), 2363–2366.
- Krehbiel, P. R., J. A. Rioussset, V. P. Pasko, R. J. Thomas, W. Rison, M. Stanley, and H. E. Edens (2008), Upward electrical discharges from thunderstorms, *Nat. Geosci.*, *1*, 233–237.
- Krider, E. P. (1992), On the electromagnetic fields, Poynting vector, and peak power radiated by lightning return strokes, *J. Geophys. Res.*, *97*, 15,913–15,917.
- Krider, E. P. (1994), On the peak electromagnetic fields radiated by lightning return strokes toward the middle-atmosphere, *J. Atmos. Electr.*, *14*, 17–24.
- Lu, G. (2006), Transient electric field at high altitudes due to lightning: Possible role of induction field in the formation of elves, *J. Geophys. Res.*, *111*, D02103, doi:10.1029/2005JD005781.
- Lyons, W. A., M. Uliasz, and T. E. Nelson (1998), Large peak current cloud-to-ground lightning flashes during the summer months in the contiguous United States, *Mon. Weather Rev.*, *126*, 2217–2233.
- Marshall, R. A., U. S. Inan, and W. A. Lyons (2007), Very low frequency sferic bursts, sprites, and their association with lightning activity, *J. Geophys. Res.*, *112*, D22105, doi:10.1029/2007JD008857.
- Marshall, R. A., U. S. Inan, and T. W. Chevalier (2008), Early VLF perturbations caused by lightning EMP-driven dissociative attachment, *Geophys. Res. Lett.*, *35*, L21807, doi:10.1029/2008GL035358.
- Mazur, V., E. Williams, R. Boldi, L. Maier, and D. E. Proctor (1997), Initial comparison of lightning mapping with operational Time-Of-Arrival and interferometric systems, *J. Geophys. Res.*, *102*(D10), 11,071–11,085.
- Mazur, V., X. M. Shao, and P. R. Krehbiel (1998), “Spider” lightning in intracloud and positive cloud-to-ground flashes, *J. Geophys. Res.*, *103*(D16), 19,811–19,822.
- Mende, S. B., H. U. Frey, R. R. Hsu, H. T. Su, A. B. Chen, L. C. Lee, D. D. Sentman, Y. Takahashi, and H. Fukunishi (2005a), D region ionization by lightning-induced electromagnetic pulses, *J. Geophys. Res.*, *110*, A11312, doi:10.1029/2005JA011064.
- Mende, S. B., H. U. Frey, H. -T. Su, R. -R. Hsu, A. B. Chen, H. Fukunishi, Y. Takahashi, T. Adachi, and L. -C. Lee (2005b), Global TLE observations with ISUAL, paper presented at Berkeley Special Seminar, Univ. of Calif., Berkeley, Calif.
- Morgan, W. L., and B. M. Penetrante (1990), ELENDF: A time-dependent Boltzmann solver for partially ionized plasmas, *Comput. Phys. Commun.*, *58*(1–2), 127–152.
- Moss, G. D., V. P. Pasko, N. Liu, and G. Veronis (2006), Monte Carlo model for analysis of thermal runaway electrons in streamer tips in transient luminous events and streamer zones of lightning leaders, *J. Geophys. Res.*, *111*, A02307, doi:10.1029/2005JA011350.
- Mur, G. (1981), Absorbing boundary conditions for the finite-difference approximation of the time-domain electromagnetic field equations, *IEEE Trans. Electromagn. Compat.*, *23*, 377–382.
- Noble, C. M. M., W. H. Beasley, S. E. Postawko, and T. E. L. Light (2004), Coincident observations of lightning by the FORTE photodiode detector, the New Mexico Tech Lightning Mapping Array and the NLDN during STEPS, *Geophys. Res. Lett.*, *31*, L07106, doi:10.1029/2003GL018989.
- Orville, R. E. (1991), Calibration of a magnetic direction finding network using measured triggered lightning return stroke peak currents, *J. Geophys. Res.*, *96*, 17,135–17,142.
- Papadopoulos, D., G. Milikh, A. Gurevich, A. Drobot, and R. Shanny (1993), Ionization rates for atmospheric and ionospheric breakdown, *J. Geophys. Res.*, *98*(A10), 17,593–17,596.
- Pasko, V. P., and U. S. Inan (1994), Recovery signatures of lightning-associated VLF perturbations as a measure of the lower ionosphere, *J. Geophys. Res.*, *99*(A9), 17,523–17,537.
- Pasko, V. P., U. S. Inan, T. F. Bell, and Y. N. Taranenko (1997), Sprites produced by quasi-electrostatic heating and ionization in the lower ionosphere, *J. Geophys. Res.*, *102*(A3), 4529–4561.
- Peter, W. B., and U. S. Inan (2005), Electron precipitation events driven by lightning in hurricanes, *J. Geophys. Res.*, *110*, A05305, doi:10.1029/2004JA010899.
- Peter, W. B., M. W. Chevalier, and U. S. Inan (2006), Perturbations of mid-latitude subionospheric VLF signals associated with lower ionospheric

- disturbances during major geomagnetic storms, *J. Geophys. Res.*, *111*, A03301, doi:10.1029/2005JA011346.
- Proctor, D. E. (1991), Regions where lightning flashes begin, *J. Geophys. Res.*, *96*(D3), 5099–5112.
- Proctor, D. E., R. Uytendogaardt, and B. M. Meredith (1988), VHF radio pictures of lightning flashes to ground, *J. Geophys. Res.*, *93*(D10), 12,683–12,727.
- Rakov, V. A., and W. G. Tuni (2003), Lightning electric field intensity at high altitudes: Inferences for production of elves, *J. Geophys. Res.*, *108*(D20), 4639, doi:10.1029/2003JD003618.
- Rakov, V. A., and M. A. Uman (2003), *Lightning: Physics and Effects*, Cambridge Univ. Press, Cambridge, U. K.
- Rowland, H. L., R. F. Fernsler, and P. A. Bernhardt (1996), Breakdown of the neutral atmosphere in the D region due to lightning driven electromagnetic pulses, *J. Geophys. Res.*, *101*(A4), 7935–7945.
- Sipler, D. P., and M. A. Biondi (1972), Measurements of  $O(^1D)$  quenching rates in the F region, *J. Geophys. Res.*, *77*, 6202–6212.
- Smith, D. A., X. M. Shao, D. N. Holden, C. T. Rhodes, M. Brook, P. R. Krehbiel, M. Stanley, W. Rison, and R. J. Thomas (1999), A distinct class of isolated intracloud lightning discharges and their associated radio emissions, *J. Geophys. Res.*, *104*, 4189–4212.
- Stanley, M., P. Krehbiel, M. Brook, C. Moore, W. Rison, and B. Abrahams (1999), High speed video of initial sprite development, *Geophys. Res. Lett.*, *26*(20), 3201–3204.
- Taranenko, Y. N. (1993), Interaction with the lower ionosphere of electromagnetic pulses from lightning: Heating, attachment, ionization, and optical emissions, Ph.D. thesis, Stanford Univ., Stanford, Calif.
- Taranenko, Y. N., U. S. Inan, and T. F. Bell (1993a), The interaction with the lower ionosphere of electromagnetic pulses from lightning: Heating, attachment, and ionization, *Geophys. Res. Lett.*, *20*(15), 1539–1542.
- Taranenko, Y. N., U. S. Inan, and T. F. Bell (1993b), The interaction with the lower ionosphere of electromagnetic pulses from lightning: Excitation of optical emissions, *Geophys. Res. Lett.*, *20*(23), 2675–2678.
- Thomas, R. J., P. R. Krehbiel, W. Rison, T. Hamlin, D. J. Boccippio, S. J. Goodman, and H. J. Christian (2000), Comparison of ground-based 3-dimensional lightning mapping observations with satellite-based LIS observations in Oklahoma, *Geophys. Res. Lett.*, *27*(12), 1703–1706.
- Uman, M. A., and D. K. McLain (1970), Lightning return stroke current from magnetic and radiation field measurements, *J. Geophys. Res.*, *75*, 5143–5147.
- Veronis, G., V. P. Pasko, and U. S. Inan (1999), Characteristics of mesospheric optical emissions produced by lightning discharges, *J. Geophys. Res.*, *104*(A6), 12,645–12,656.
- Villanueva, Y., V. A. Rakov, M. A. Uman, and M. Brook (1994), Microsecond-scale electric field pulses in cloud lightning discharges, *J. Geophys. Res.*, *99*(D7), 14,353–14,360.

---

V. S. Glukhov, Liquidnet Holdings, Inc., 498 Seventh Ave., New York, NY 10018, USA.

U. S. Inan and R. A. Marshall, Space, Telecommunications and Radioscience Laboratory, Stanford University, 350 Serra Mall, Rm. 306, Stanford, CA 94305, USA. (ram80unit@gmail.com)